Aerosol Science and Technology

ISSN: (Print) (Online) Journal homepage: www.tandfonline.com/journals/uast20

First complex refractive indices retrieval from FIR to UV: Application to kaolinite particles

Maria Chehab, Hervé Herbin, Alexandre Deguine, Sylvie Gosselin, Valentine Bizet & Denis Petitprez

To cite this article: Maria Chehab, Hervé Herbin, Alexandre Deguine, Sylvie Gosselin, Valentine Bizet & Denis Petitprez (2024) First complex refractive indices retrieval from FIR to UV: Application to kaolinite particles, Aerosol Science and Technology, 58:5, 498-511, DOI: 10.1080/02786826.2024.2318371

To link to this article: https://doi.org/10.1080/02786826.2024.2318371

AEROSOL SCIENCE AND TECHNOLOGY
2024, VOL. 58, NO. 5, 498–511
https://doi.org/10.1080/02786826.2024.2318371

First complex refractive indices retrieval from FIR to UV: Application to kaolinite particles

Maria Chehab[a,b], Hervé Herbin[a], Alexandre Deguine[a,b]*, Sylvie Gosselin[b], Valentine Bizet[b], and Denis Petitprez[b]

[a]Univ. Lille, CNRS, UMR 8518 - LOA - Laboratoire d'Optique Atmosphérique, Lille, France; [b]Univ. Lille, CNRS, UMR 8522 - PC2A - Physicochimie des Processus de Combustion et de l'Atmosphère, Lille, France

ABSTRACT

Knowledge of the optical properties, in particular the complex refractive indices (CRI), of aerosols is crucial to better quantify their impact on the environment from remote sensing techniques. However, the CRI data available in the literature provide mainly reflectance measurements on bulk materials or pressed pellets and span over limited wavelength ranges. Here, we present an improved retrieval methodology combining an experimental setup that allows simultaneously the measurement of high spectral-resolution extinction spectra (up to 0.5 cm^{-1}) and the recording of the size distribution (SD) of both fine (down to 10 nm) and coarse (up to 20 μm) particles. Introducing these experimental measurements in a numerical iterative process, the real and imaginary parts of the CRI are retrieved using an optimal estimation method (OEM) associated with scattering theories and the single subtractive Kramers–Kronig (SSKK) relation. Using this methodology, we are able to accurately determine for the first time CRI of an aerosol flow for kaolinite over a wide spectral range from far infrared (FIR) (50 μm/200 cm^{-1}) up to UV (0.25 μm/40,000 cm^{-1}). The mean values of the total uncertainty of the retrieved real and imaginary parts are 1.6% and 0.6%, respectively.

GRAPHICAL ABSTRACT

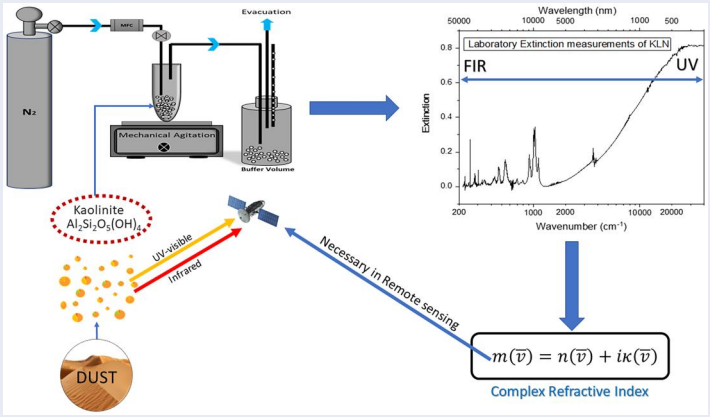

ARTICLE HISTORY
Received 5 September 2023
Accepted 30 January 2024

EDITOR
Hans Moosmüller

1. Introduction

Mineral dust aerosols are the most abundant aerosol type by mass emitted into the atmosphere (5000 Tg y^{-1}, Kinne et al. 2006; Kok et al. 2017) via natural processes such as wind erosions (Méndez Harper et al. 2022). Due to their ability to absorb and scatter solar radiation, major injections of these particles can have a significant effect on the atmosphere including changes in temperature and precipitation patterns, and impacts on the radiation balance of the Earth (Osborne et al. 2011; Satheesh and Moorthy 2005). Given the variability and spatial heterogeneity of their

CONTACT Maria Chehab maria.chehab@univ-lille.fr Univ. Lille, CNRS, UMR 8518 - LOA - Laboratoire d'Optique Atmosphérique, F-59000 Lille, France.
*Current affiliation: Université du Littoral Côte d'Opale, UR 4493, Laboratoire de Physico-Chimie de l'Atmosphère, Dunkerque, France

Supplemental data for this article can be accessed online at https://doi.org/10.1080/02786826.2024.2318371.

concentration, size, and chemical composition, it is important to quantify these aerosols in order to better identify their sources and understand their environmental impact from regional to global scale. Ground-based networks such as EARLINET (www.earlinet.org) use Lidar to acquire physical information such as height and plume thickness and AERONET (https://aeronet.gsfc.nasa.gov) uses sun photometers to obtain optical information, mainly aerosol optical depth (AOD). Dedicated satellite instruments for instance MISR, Polder, or MODIS can derive information regarding AOD as well as regional trends of combustion and dust aerosols (Yu et al. 2020) and radiative forcing. However, a better characterization of the aerosol, such as obtaining chemical, mineralogical, and microphysical (concentration, size distribution [SD]) aerosol properties, requires accurate information about the complex refractive index (CRI) $m(\overline{\nu}) = n(\overline{\nu}) + i\kappa(\overline{\nu})$, where $(\overline{\nu})$ denotes spectral wavenumber, $n(\overline{\nu})$ and $\kappa(\overline{\nu})$ represent the real and the imaginary part of the refractive index respectively. Indeed, whatever the type of measurement is, the algorithms used to retrieve particle parameters require aerosol models that depend on CRIs. Although not historically dedicated to aerosol studies, hyperspectral and high spectral resolution infrared instruments, such as the Atmospheric Infrared Sounder (AIRS) and the Infrared Atmospheric Sounding Interferometer (IASI), combined with precise CRI datasets, have demonstrated their efficiency in determining chemical composition (Alalam et al. 2022) and microphysical parameters (Clarisse et al. 2010; Deguine et al. 2023b) of aerosols. It is, therefore, necessary to improve our knowledge regarding CRIs for better exploitation of current and upcoming infrared satellite instruments such as the IASI-NG, IRS-MTG, and in particular the FORUM mission which will be launched in 2027. Indeed, the latter will perform far infrared (FIR) measurements, a spectral region for which information regarding CRIs is very limited. We can also add that in the context of inter-instrument comparison exercises or the use of instrumental synergies it is essential to have homogeneous CRI data over the widest possible spectral range (Chen et al. 2022).

Literature datasets give the optical constants of minerals obtained from bulk materials or pellet techniques (Egan 2012; Glotch, Rossman, and Aharonson 2007; Longtin et al. 1988). Using pellet techniques has several limitations such as the modification of the microphysical properties of the particles (SD and morphology). Furthermore, in pellet samples, the particles are present in a compressed matrix causing modifications of the vibrational modes. For bulk measurements, there is a strong underestimation of the scattering signal. Therefore, as explained by McPheat et al. (2002) and deduced from the works of Mogili et al. (2007) and Reed et al. (2017), these types of measurements are not representative of atmospheric aerosols and in turn are not suitable for aerosol CRI retrieval, in particular in the infrared. Recently, a few research facilities have been implementing a new methodology for the retrieval of CRI of aerosols by using laboratory resuspension and SD measurements (Di Biagio et al. 2019; Engelbrecht et al. 2016; Mogili et al. 2008; Reed et al. 2017). Among these approaches, our method has already shown its efficiency on multiple dust aerosols such as amorphous and crystalline silica (Quartz) as well as volcanic ashes (Deguine et al. 2023a; Herbin et al. 2023; Hubert et al. 2017). Since then, modifications and improvements have been established such as the extension of spectral coverage by adding a new breadboard capable of measuring FIR extinction spectra from 100 to 650 cm^{-1}, and optimization of our numerical formulation for a finer and faster retrieval.

This experimental system has been used in this work to measure the CRI of kaolinite ($Al_2O_3{\cdot}2SiO_2{\cdot}2H_2O$), also known as aluminum silicate which is a layered silicate clay mineral formed from the dissolution of rocks rich in feldspar and aluminum silicate minerals. It is a 1:1 dioctahedral phyllosilicate mineral where each kaolinite layer has one alumina octahedral sheet and one silica tetrahedral sheet (Varga 2007). It is one of the most abundant minerals present in clays and can be found mainly in tropical climates having high humidity (Hoshino, Sanematsu, and Watanabe 2016). Clay minerals contribute to two-thirds of dust mass, whereas kaolinite alone contributes up to 13% (Atkinson et al. 2013). Although kaolinite is a significant component of atmospheric mineral dust aerosols produced by dust storms, its laboratory extinction/absorption spectrum is not often measured and if done, it is with low spectral resolution compared to satellite observations (Balan et al. 2001; Laskina et al. 2012; Mogili et al. 2007). Datasets for the CRI of kaolinite are presented in Figure 1, however, each is over a limited spectral range (Arakawa et al. 1997; Egan 2012; Glotch, Rossman, and Aharonson 2007; Querry 1998; Roush, Pollack, and Orenberg 1991). CRI datasets from Glotch, Rossman, and Aharonson (2007), Roush, Pollack, and Orenberg (1991), and Querry (1998) are in the infrared region alone, ranging between 100–2000, 400–2000, and 50–4000 cm^{-1}, respectively. As for Arakawa et al. (1997) and Egan

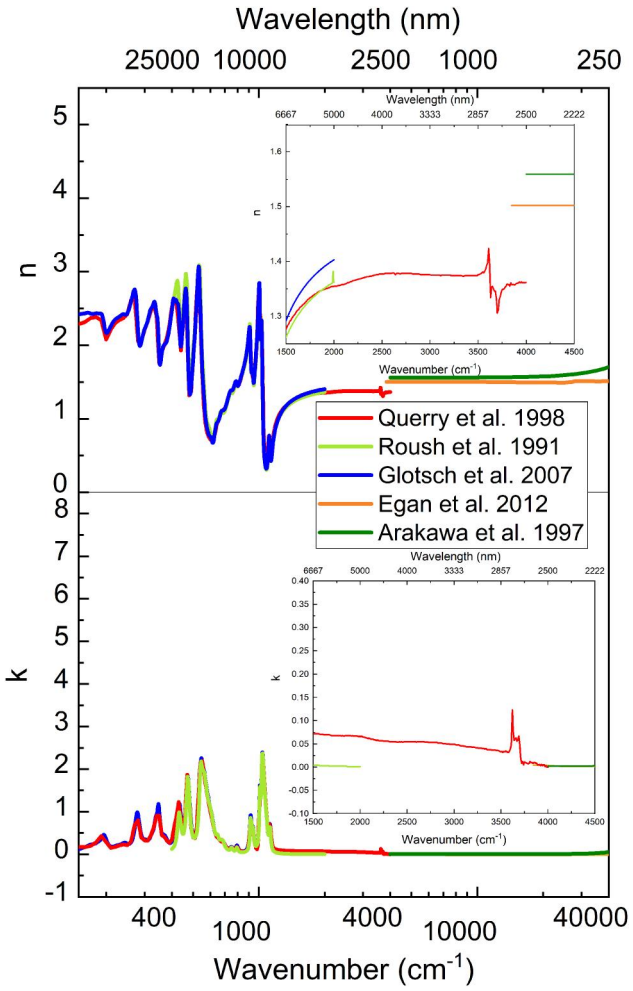

Figure 1. Literature values of the real part (top) and the imaginary part (bottom) of complex refractive indices of kaolinite. The inset shows a zoomed portion between 1500 and 4000 cm^{-1} highlighting the region with the most inconsistencies.

(2012), their sets are in the range of 4000–77,000 cm^{-1} and 4000–54,000 cm^{-1}, respectively, covering the near-infrared (NIR) and UV–visible regions. The CRIs coming from these different measurements are also not consistent with each other. For example, at $\bar{\nu} = 4000\,cm^{-1}$, measurements from Arakawa et al. (1997) of the real part (top figure) of the refractive index show $n(\bar{\nu}) = 1.559$ while measurements done by Egan (2012) and Querry (1998) have lower values of 1.502 and 1.362, respectively. The inconsistencies in the CRI of kaolinite can be a major obstacle in its characterization by remote sensing techniques.

The present work describes the experimental and theoretical procedure allowing the retrieval of a continuous CRI set for crystalline kaolinite from FIR (200 cm^{-1}) up to UV (40,000 cm^{-1}). The following section gives a brief explanation of the experimental setup being used with the respective results. Some of the changes since Herbin et al. (2023) will be highlighted, specifically the addition of a new spectrometer breadboard allowing spectral recordings in the FIR region. Section 3 details the new numerical procedure as well as the final retrieved set of CRI of kaolinite and their uncertainties. Finally, Section 4 summarizes our results and presents perspectives for future works and applications.

2. Experimental setup

The experimental setup, shown in Figure 2, can be divided into three main parts: 1- aerosol generation used for sample resuspension, 2- spectrometers, one for the IR region while the other for the UV–visible region, and 3- two particle sizers used to record the SD of the particles. The setup has already been presented in previous articles (Deguine et al. 2020; Herbin et al. 2023; Hubert et al. 2017) and is only briefly recalled here highlighting some improvements, especially in the FIR region.

2.1. Aerosol generation

The kaolinite sample is provided by Sigma-Aldrich (CAS number 1318-74-7). It has a density equal to 2.65 $g.cm^{-3}$ (Varga 2007). First, we place it in a Petri dish in an oven of temperature 353 K for at least 12 h to remove water residues at the surface of the particles. The particles are then introduced into a glass reactor containing a bar magnet for mechanical agitation of 1500 revolutions.min^{-1} causing the resuspension of the particles. They are carried away in a constant flow of 3 $L.min^{-1}$ of nitrogen (N_2, purity 99.996%) managed by a mass flow controller. Downstream, a 1 L buffer volume is used to achieve a stable concentration and uniform SD of aerosols, throughout the full acquisition period. This also makes it possible to impact large particles which, otherwise, would have been deposited in the spectrometers' cells. Piping connections are as short and as straight as possible to limit particle losses. Before extinction measurement, the system is purged with N_2 for at least 4 h to minimize as much as possible the absorption bands coming from water vapor and carbon dioxide in the interferometer and cells. Using a fixed nitrogen flow rate with an occasional pulsing of the flow every 5–10 s and a controlled variation of the mechanical agitation, the concentration of particles remains stable enough for the full acquisition time where the variability of the concentration during the experiment is less than 5%.

2.2. Extinction measurements

The resuspended particles pass through the cells of the spectrometers for extinction spectra recording. The first cell crossed by the sample is a 10 m multi-pass cell placed horizontally in the Fourier Transform InfraRed (FTIR) spectrometer (iS50 from Thermo Scientific) to minimize particle sedimentation on the mirror. To cover the FIR region, a new breadboard has been recently installed with another 10-m multi-pass cell with polyethylene (PE) windows, a DTGS detector, and a Solid Substrate beam splitter. To be able to add this new optical element, modifications to the original infrared breadboard needed to be made as well as changes in the aerosol trajectory inside the system. Since the CO_2 and H_2O absorption are high in the FIR region, purging time is increased to 5 h before resuspension to remove the residual traces of these compounds. The particles then pass through a cell (1 m-length and 48 mm-diameter) placed in a UV–visible spectrometer composed of 2 light sources, a deuterium lamp and a halogen lamp, emitting from 210 to 400 nm and from 360 to 1500 nm, respectively.

Table 1 shows the best configuration of windows, beam-splitters, and detectors to get extinction spectra from 100 cm^{-1} up to 50,000 cm^{-1}. In the infrared and UV–visible regions, we were able to collect extinction measurements with high spectral resolutions of 0.5 cm^{-1} and 1 nm, respectively. The collection of data takes 180 s. The acquisition time is optimized to compensate for getting enough sensitivity from the spectrometers for a good signal-to-noise ratio and minimizing the deposition of particles on the mirrors and windows of the cells. The experimental extinction spectrum of kaolinite is shown in Figure 3.

Due to the large amount of noise at the beginning of the FIR spectral range as well as at the end of the UV–visible range, we limit our region of study between $\overline{\nu}_l = 200$ and $\overline{\nu}_h = 40{,}000\ cm^{-1}$. Moreover, although purging is done to reduce H_2O vapor and CO_2 molecules, there are still some residues coming from the sample desorption. The latter produces spectral features (gaseous absorption lines) that must be removed in order to not disturb the CRI retrieval. This procedure is performed by a Savitzky–Golay smoothing method (Savitzky and Golay 2002), which reduces the amplitude of high-frequency signal coming from gaseous residues and instrumental noise (see the red curve of Figure 3) and makes it possible to distinguish the main extinction peaks.

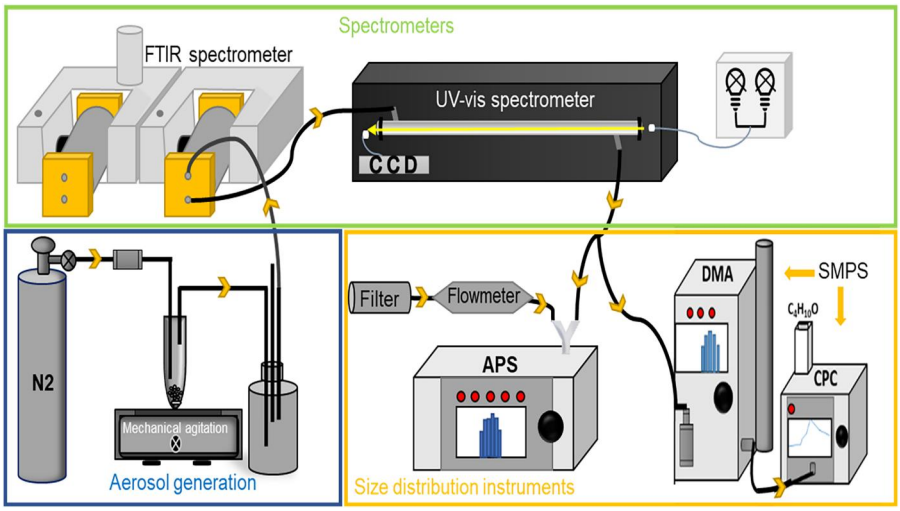

Figure 2. Schematic representation of the experimental setup used. It is composed of an aerosol generation system (blue box), FTIR and UV–visible spectrometers (green box), an Aerodynamic Particle Sizer (APS) spectrometer and a Scanning Mobility Particle Sizer (SMPS) made of a Differential Mobility Analyzer (DMA) and a Condensation Particle Counter (CPC) (yellow box).

Table 1. List of detectors, beam-splitters, and windows used in the spectrometers as well as the corresponding spectral range.

Spectral range (cm^{-1})	Detector	Beam splitter	Windows of the cell	Spectral resolution
100–650	DTGS	Solid substrate	Polyethylene	0.5 cm^{-1}
650–4000	MCT	KBr	BaF_2	0.5 cm^{-1}
4000–8000	InGaAs	CaF_2	BaF_2	0.5 cm^{-1}
9000–50,000	CCD		Quartz	1 nm

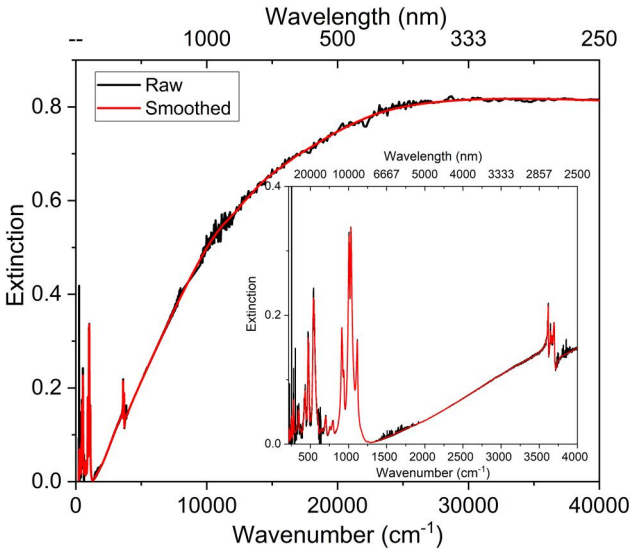

Figure 3. Extinction spectrum of kaolinite between 200 and 40,000 cm^{-1}. The black curve represents the experimental extinction spectrum while the red curve shows the smoothed version. The inset shows a zoomed portion between 200 and 4000 cm^{-1} highlighting the region from far infrared to middle infrared.

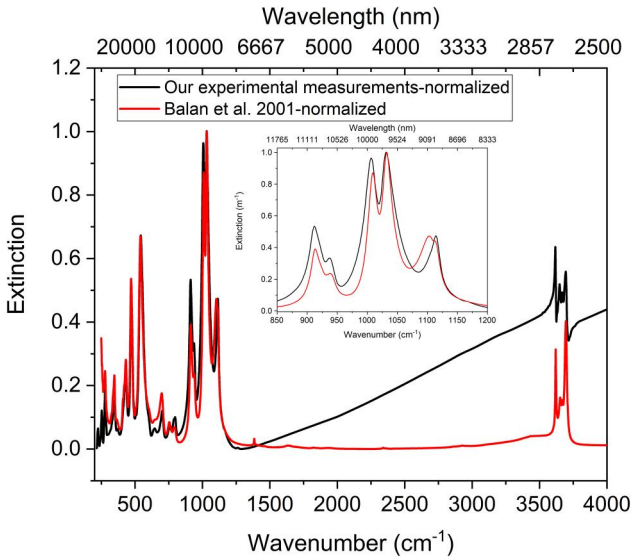

Figure 4. Comparison between the experimental absorbance spectrum of Balan et al. (2001), our extinction spectrum in the IR regions. The inset shows a zoomed portion between 850 and 1200 cm^{-1} highlighting the peak shifts between the two datasets.

The two prominent bands at 473 and 542 cm^{-1} are due to the bending vibrations of Si-O-Al^{VI} and Si-O-Si groups, respectively (Madejová, Gates, and Petit 2017). Weak bands at 702 and 756 cm^{-1} are related to the perpendicular Si-O vibrations involving the surface hydroxyl layer. The Al_2OH bending vibrational modes at 912 and 937 cm^{-1} arise from vibrations of inner and inner-surface OH groups, respectively. The modes at 1007 and 1031 cm^{-1} are caused by the antisymmetric in-plane Si-O-Si stretching vibrations. The high-frequency band at 1114 cm^{-1} is assigned to the symmetric stretching Si-O vibrations involving the basal oxygens. The OH stretching region of kaolinite shows 4 resolved bands at 3617, 3649, 3668, and 3694 cm^{-1}. The 3617 cm^{-1} vibrational mode arises from the vibrational stretching of single "inner" hydroxyl groups (ν_{OH}) bonded to octahedral cations while the others are due to coupled vibrational stretching of nonequivalent "inner-surface" OH groups located at the surface of the dioctahedral sheet of the layers (Madejová, Gates, and Petit 2017). Figure 4 compares the normalized experimental absorbance obtained by Balan et al. (2001) to our smoothed extinction measurements. We can notice a good agreement between our assignment and that of Balan et al. (2001), whose experimental setup uses a pellet sample. Nevertheless, although peak positions between the experiment from Balan et al. (2001) and ours are consistent, they are not identical. First, it is due to the fact that the transmission IR spectrum of the kaolinite pellet of Balan et al. (2001) was recorded with a coarser spectral resolution (2 cm^{-1}). Then, the kaolinite particle size of Balan et al. (2001) is roughly 0.7 µm, much larger than the mean diameter measured by our experiment, which leads to a systematic spectral shift.

There are also differences in the intensity ratios which are explained by the fact that Balan et al. (2001) uses the pellet technique instead of using resuspension of particles. Finally, some features in FIR and MIR (225, 240, 253, 506, and 788 cm^{-1}) were not detected by Balan et al. (2001) but were predicted by their ab initio calculations.

2.3. Size distribution determination

SDs of the particles were measured by an aerodynamic particle sizer (APS, TSI 3321) and a scanning mobility particle sizer (TSI SMPS 3936L75).

The APS's principle is based on the measurement of the time of flight of a particle. It measures the SD for aerodynamic diameters D_a between 0.523 and 20 µm where D_a is the equivalent diameter of a spherical particle that falls in the air at the same speed as the non-spherical particle being studied. A measured SD by the APS of the kaolinite sample is represented by black bins in Figure 5.

The SMPS is used to measure finer particles. It couples a differential mobility analyzer (TSI DMA 3080) that selects particles based on their electric mobility, with a condensation particle counter (TSI

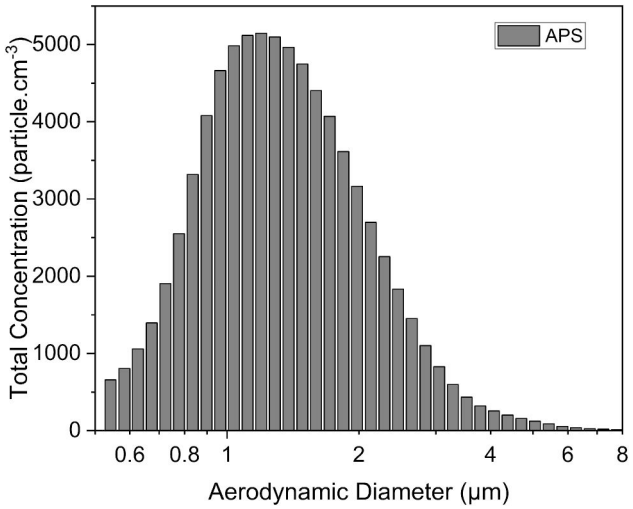

Figure 5. The total concentration measurements with respect to the aerodynamic diameter recorded by the APS considering the dilution factor.

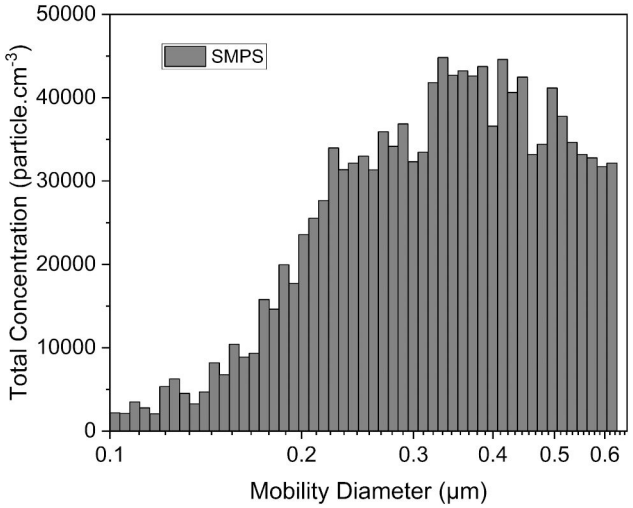

Figure 6. The total concentration measurements with respect to the mobility diameter recorded by the SMPS.

CPC 3775) that detects the selected particles. In the DMA, particles with positive charge move toward the internal electrode to pass through the exit slot. These selected particles are then integrated into the CPC at a 0.3 L.min^{-1} rate where the volume of each particle is increased by condensed vapors of butanol making them optically detectable droplets. The SMPS, depending on the impactor used, records the electrical mobility diameter D_m of particles varying between 10 and 800 nm. The SD measurement of kaolinite by the SMPS is given in Figure 6.

As part of the CRI retrieval process, we need a SD associated with the experimental extinction spectrum. The SD is described by parameters called moments of distribution which are the total number concentration N_t (in #.cm^{-3}), the geometric standard deviation σ_g, and the volume equivalent mean diameter $\overline{D}$ (in µm). The log-normal law is a mathematical expression (Seinfeld and Pandis 2006) that models the SD of atmospheric aerosols and is presented in Equation (1) where N is the concentration and D is the diameter of the particle:

$$n(D) = \frac{dN}{d\log(D)} = \frac{N_t}{\sqrt{2\pi}\log\sigma_g}\exp\left(\frac{-\left(\log D - \log\overline{D}\right)^2}{2\left(\log\sigma_g\right)^2}\right) \quad (1)$$

We have recorded two SDs coming from two different devices. To link these two measurements, we consider the volume equivalent diameter D_{ve}. Equations (2) and (3) relate the volume equivalent diameter to the aerodynamic diameter and the mobility diameter, respectively (DeCarlo et al. 2004).

$$D_{ve} = D_a\left(\frac{\rho_0\chi C_c(D)}{\rho C_c(Dve)}\right)^{\frac{1}{2}} \quad (2)$$

$$D_{ve} = D_m\left(\frac{C_c(Dve)}{C_c(D_m)\chi}\right) \quad (3)$$

where ρ_0 and ρ are the densities (in g.cm^{-3}) of water and the particle, respectively, χ is the shape factor of the particle while Cc represents the Cunningham slip factor of either the volume equivalent diameter, the aerodynamic diameter or the mobility diameter (Kim et al. 2005). By using a similar method as used by Herbin et al. (2023) and described by Khlystov, Stanier, and Pandis (2004), which consists of determining χ by fitting Equation (4) from the experimental data D_m from the SMPS and D_a from the APS in the area where the diameters overlap, we can estimate the shape factor to $\chi \approx 3$.

$$D_m = D_a\sqrt{\chi\frac{C_c(D_a)\rho_0}{C_c(D_m)\rho}} \quad (4)$$

This shape factor value corresponds to very irregular particles, which is consistent with the typical shape of kaolinite generally described by an overall hexagonal appearance (Tunega and Zaoui 2020).

The drop in the counting efficiency of APS for sizes lower than 1 µm, the fact that the χ factor is only roughly estimated, and the particle losses in the setup, specifically the fine particles lost by diffusion, especially on spectrometer mirrors and windows, as well as coarse particles lost by sedimentation, are the main sources of uncertainties in the determination of the moments of distributions. Therefore, the latter

have to be optimized before being able to use them for the CRI retrieval process. The moments of distribution are adjusted using a least square fit method with respect to the experimental extinction spectrum in the UV region. This operation is done in the spectral range between 4000 and 40,000 cm^{-1} where the extinction spectrum is mainly governed by the real part of the CRI having monotonic behavior and relatively independent of the experimental method used (pellets, bulk, or suspended particles). The optimization method is similar to that of Mogili et al. (2007). This method needs a priori values of the SD parameters. For that, we used the values obtained from the log-normal fit of the experimental measurements from SMPS and APS. A literature set of optical constants in this spectral range can also be useful for this operation. According to Arakawa et al. (1997), the CRIs obtained from Egan (2012) are low due to the fact that they were not able to collect a large fraction of scattered light. Therefore, the Arakawa et al. (1997) dataset is chosen for the optimization procedure.

The latter uses Mie theory to simulate an extinction spectrum using the a priori SD parameters and the literature complex refractive indices (CRI) in an iterative process. The new optimized moments of distribution are $N_t = 1.504 \times 10^6$ cm^{-3}, $\overline{D} = 0.118\,\mu m$; $\sigma_g = 2.340$. To verify the retrieved SD parameters, a spectrum is also simulated within the framework of geometric optics since at high wavenumbers geometric optics depends mainly on the particle SD parameters (Nussenzveig and Wiscombe 1980). As shown in Figure 7, the consistency between Mie theory simulation, geometric optics calculation, and the raw experimental data around 40,000 cm^{-1} validate the optimized SD parameters.

3. CRI retrieval

The numerical procedure carried out to retrieve CRIs has been thoroughly explained by Herbin et al. (2017). Modifications to the numerical formulations have been introduced since then, such as the use of logarithmic calculations, changing the a priori set, and enhancing the convergence criteria to refine the retrieved data. The new numerical protocol is summarized in the flowchart of Figure 8. The following section will briefly recapture the main points since Herbin et al. (2017) as well as highlight the changes and improvements made and the final results obtained.

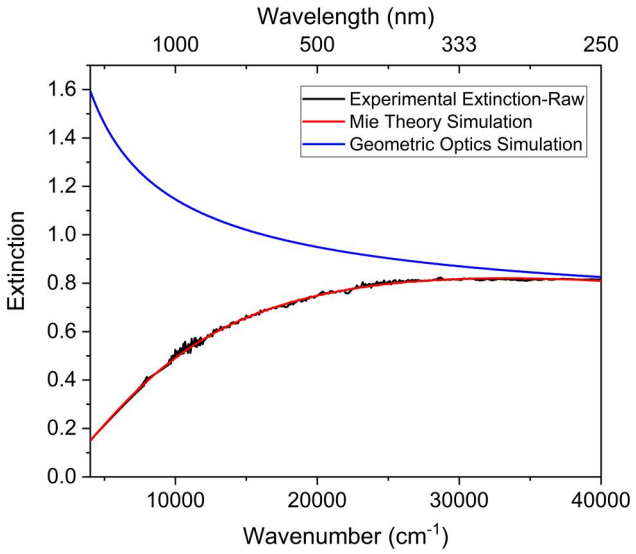

Figure 7. Comparison of the raw experimental data from 4000 to 40,000 cm^{-1} (in black) to the Mie theory simulation (in red) and the simulation from the geometric optics calculations (in blue).

3.1. CRI retrieval using the optimal estimation method

Even if the extinction spectrum is well obtained and the SD parameters are optimized to the best possible values, it's difficult to retrieve two unknowns (n and κ) at each wavenumber. For this reason, we use the optimal estimation method (OEM) (Rodgers 2000) and the single subtractive Kramers–Kronig (SSKK) relation expressed in Equation (5) which adds a correlation between n and κ.

$$n(\overline{\nu}) - n(\overline{\nu}_a) = \frac{2(\overline{\nu}^2 - \overline{\nu}_a{}^2)}{\pi} P\int_0^{\infty} \frac{\overline{\nu'}k(\overline{\nu'})}{\left(\overline{\nu'}^2 - \overline{\nu}^2\right)\left(\overline{\nu'}^2 - \overline{\nu_a}^2\right)} d\overline{\nu'} \tag{5}$$

In the former equation, $\overline{\nu}_a$ represents the wavenumber of the anchor point for which the real part of the refractive index, $n(\overline{\nu}_a)$, is fixed and P is the principal Cauchy value of the integral. The goal of OEM is to obtain the best estimation $\hat{x}$, of the state vector x composed of $n(\overline{\nu})$ and $\kappa(\overline{\nu})$ values we wish to determine, by regularizing the retrieval with a priori information x_a about the variables as well as their a priori variability S_a. The iterative process of the OEM has been recently refined since Herbin et al. (2023) by using the logarithmic formulation instead of linear. This is done because logarithmic scale proved to be better for inversion processes involving a wide-reaching range in the retrieved parameters and between the measurements and the numerical values of the state

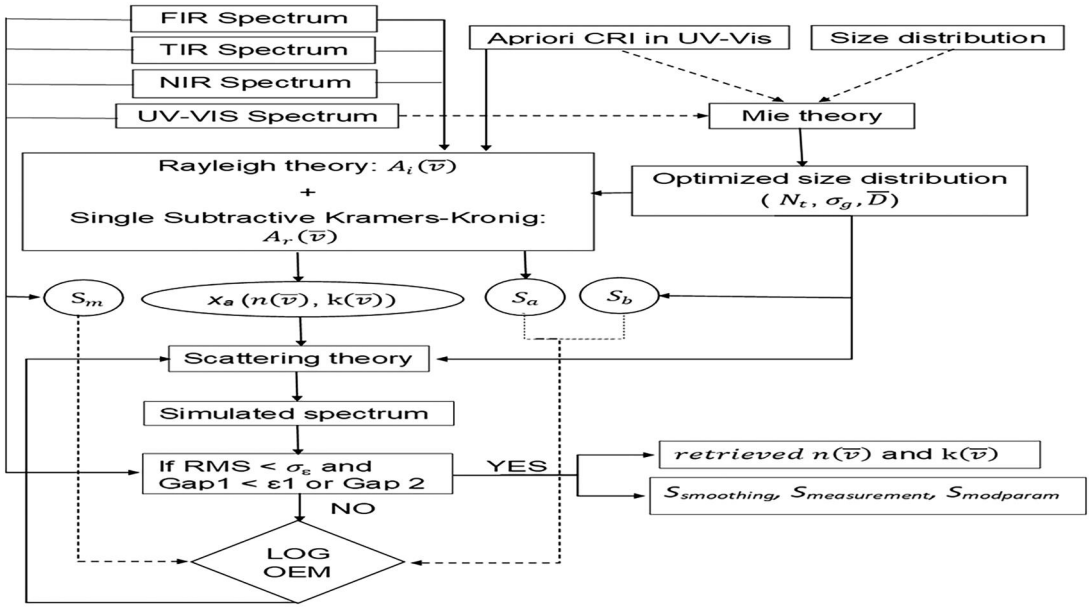

Figure 8. Flowchart of the algorithm used for the CRI retrieval.

vector. This refined version of the iterative process is given in Equation (6).

$$ln\hat{x}_{i+1} = lnx_a + \left(K_i^T S_{\in}^{-1}{}_i + S_a^{-1}\right)^{-1} K_i^T S_{\in}^{-1} \times \left[y - F(\hat{x}_i) + K_i(ln\hat{x}_i - lnx_a)\right] \quad (6)$$

In Equation (6), y represents the experimentally measured extinction spectrum, F is the forward model, i.e. scattering theory, $K = \frac{\partial F}{\partial ln\hat{x}}$ is the Jacobian matrix and K^T is its transpose. S_a is estimated from the difference between the experimental extinction and the simulated one using x_a (Herbin et al. 2023). S_ε is a variance-covariance matrix equal to $S_m + K_b S_b K_b^T$ that estimates the average noise from the instrument S_m and the errors S_b relating to the non-retrieved SD parameters b. In this case, $K_b = \frac{\partial F}{\partial lnb}$ is the Jacobian matrix corresponding to the sensitivity of the forward model with respect to b.

The first step in the retrieval process is finding a priori vector x_a. Previously, the a priori set for OEM was formed by $\kappa(\bar{\nu})$ and $n(\bar{\nu})$ values, however, this set has been recently updated to include $A_i(\bar{\nu})$ and $A_r(\bar{\nu})$ values, the imaginary and real part of the spectrum, respectively, instead for an optimized retrieval. To do so we use the Rayleigh approximation in the IR region. Assuming a dispersed homogeneous medium, $A_i(\bar{\nu})$ can be represented as:

$$A_i(\bar{\nu}) = \frac{y}{6\pi\bar{\nu} f_v L} \quad (7)$$

f_v is the volume fraction of the particles and L is the length of the optical path in cm. The Rayleigh theory algorithm calculates the value of $A_i(\bar{\nu})$ and then the SSKK integration calculates $n(\bar{\nu})$ at each wavenumber. Since we use SSKK in the retrieval methodology of CRI, a constant spectral grid is needed. Therefore, before applying the Rayleigh approximation, to homogenize, we interpolate with the same spectral grid of $1\,cm^{-1}$. An anchor point corresponding to the real component of the refractive index at a specific wavenumber is needed. For our purpose, we have chosen the anchor point $n(\bar{\nu}_a) = 1.559$ at wavenumber $\bar{\nu}_a = 5000\,cm^{-1}$ since the real part $n(\bar{\nu})$ has a monotonic variability in this region and the sensitivity of the measurement is maximum for $n(\bar{\nu})$ and minimum for $\kappa(\bar{\nu})$ (Herbin et al. 2017). Since Rayleigh is only a good approximation in the IR region, the iterative process is limited between $200\,cm^{-1}$ and the wavenumber corresponding to the minimum extinction which in our case is $1293\,cm^{-1}$. To avoid discontinuity at the ends of the spectral ranges, extrapolation of $A_i(\bar{\nu})$ is made using the following relations (Herbin et al. 2017):

$$A_i(\bar{\nu}) = \frac{A_i(\bar{\nu}_l) \times \bar{\nu}}{\bar{\nu}_l} \quad (0 < \bar{\nu} < \bar{\nu}_l) \quad (8)$$

$$A_i(\bar{\nu}) = \frac{A_i(\bar{\nu}_h) \times \bar{\nu}_h{}^3}{\bar{\nu}^3} \quad \left(\bar{\nu}_h < \bar{\nu} < \bar{\nu}_{\max} = 50{,}000\ cm^{-1}\right) \quad (9)$$

In the NIR region, since there are both absorption and scattering, Rayleigh's theory is thus not able to reproduce the extinction band of kaolinite. Therefore, between 3500 and $3800\,cm^{-1}$, an absorption spectrum from literature is needed to have a priori values of

$A_i(\overline{\nu})$. The absorption spectra from Balan et al. (2001) is used to extract the imaginary part of the refractive index in that region of the spectrum.

The Rayleigh algorithm uses an iterative process to calculate the refractive index at each iteration over the full spectral range. It uses the a priori values x_a made up of $A_i(\overline{\nu})$ and $A_r(\overline{\nu})$ in the iterative process where $A_r(\overline{\nu})$ is an analytic function and can be rewritten as a KK-like relationship:

$$A_r(\bar{\nu}) \approx 1 - \frac{3}{2 + n(\bar{\nu}_a)^2} + \frac{2\left(\bar{\nu}^{-2} - \bar{\nu}_a^{-2}\right)}{\pi} P \int_{\bar{\nu}_l}^{\bar{\nu}_h} \frac{\overline{\nu'} A_i(\overline{\nu'})}{(\nu'^2 - \bar{\nu}^2)(\nu'^2 - \bar{\nu}_a^2)} d\overline{\nu'} \tag{10}$$

After having an initial first guess of the real and imaginary part of the spectrum, an inversion process is used to optimize these a priori values (Herbin et al. 2017). The dielectric function's real $\in_r(\overline{\nu})$ and imaginary parts $\in_i(\overline{\nu})$ are used to calculate the real and imaginary parts of the refractive index:

$$\in_r(\overline{\nu}) = \frac{3(1 - A_r(\overline{\nu}))}{(1 - A_r(\overline{\nu}))^2 + A(\overline{\nu})^2} - 2 \tag{11}$$

$$\in_i(\overline{\nu}) = \frac{3A_i(\overline{\nu})}{(1 - A_r(\overline{\nu}))^2 + A_i(\overline{\nu})^2} \tag{12}$$

Knowing that $\in_r(\overline{\nu}) = n(\overline{\nu})^2 - k(\overline{\nu})^2$ and $\in_i(\overline{\nu}) = 2n(\overline{\nu})k(\overline{\nu})$, the real and imaginary part of the complex refractive index are calculated by:

$$n(\overline{\nu}) = \left[\frac{(\in_r(\overline{\nu})^2 + \in_i(\overline{\nu})^2)^{\frac{1}{2}} + \in_r(\overline{\nu})}{2}\right]^{\frac{1}{2}} \tag{13}$$

$$\kappa(\overline{\nu}) = \left[\frac{(\in_r(\overline{\nu})^2 + \in_i(\overline{\nu})^2)^{\frac{1}{2}} - \in_r(\overline{\nu})}{2}\right]^{\frac{1}{2}} \tag{14}$$

Using $n(\overline{\nu}), k(\overline{\nu})$, and Mie theory, we can simulate an extinction spectrum. The values of $A_i(\overline{\nu})$ are then adjusted during an iterative loop that minimizes the difference between the experimental extinction found in the laboratory and the simulated one. This difference is then related to the difference in $A_i(\overline{\nu})$ values that is then added to the next value of $A_i(\overline{\nu})$.

$$\Delta A_i(\overline{\nu})_j = \frac{(ExperimentalExtinction(\overline{\nu}) - SimulatedExtinction(\overline{\nu}))}{6\pi\overline{\nu}fL} \tag{15}$$

$$A_i(\overline{\nu})_{j+1} = A_i(\overline{\nu})_j + \Delta A_i(\overline{\nu})_j \tag{16}$$

After each new value of $A_i(\overline{\nu})$, a set of values of the real and imaginary parts of the refractive index is calculated to simulate a new extinction spectrum. The iterative process is conditioned to stop based on a limit value on the RMS as well as on its deviations:

$$Gap1_{j+1} \leq \frac{RMS_j - RMS_{j+1}}{RMS_j} \tag{17}$$

or

$$Gap2_{j+1} \leq \frac{RMS_{j-1} - RMS_{j+1}}{RMS_{j-1}} \tag{18}$$

This is done to ensure that at each iteration, the RMS is improving and that we are in the global minimum instead of a local minimum. For our purposes, we conditioned the algorithm to stop when Gap1 and Gap2 decreased from the empirical values 0.02 and 0.04 respectively. These values have been chosen as a compromise between having satisfactory comparison between simulated and experimental extinction and fair calculation time of the algorithm.

Figure 9 shows the comparison of the simulated extinction using Rayleigh theory with the experimental extinction in the infrared region. After the iterative process, a set of $\kappa(\overline{\nu})$ and n $(\overline{\nu})$ values is capable of reproducing a satisfactory simulated extinction spectrum compared to the experimental one having a root mean square (RMS) value equal to 9.25 10^{-4} in the IR region which is below the estimated measurement noise. This validates the a priori x_a which will be used in Equation (6).

As stated previously, for OEM, other than a priori values of the CRI we also need a priori matrix S_a. This matrix is assumed to be a diagonal matrix where its diagonal elements are defined by Equation (19) (Herbin, Labonnote, and Dubuisson 2013).

$$S_{a,ii} = \sigma^2{}_{a,i} \quad \text{with} \quad \sigma_{a,i} = x_{a,i} \times \frac{P_{\text{error}}}{100} \tag{19}$$

$\sigma_{a,i}$ is the standard deviation in the Gaussian statistic formalism and P_{error} is the error of the a priori values given by Rayleigh and is fixed at 2% in this study. We have also chosen the a priori uncertainty on the size parameters S_b to be 1% for each SD parameter. At the end of the iterative process of OEM, we obtain a set of CRI from which a simulated spectrum is calculated using Mie theory and compared to the experimental one in Figure 10. The RMS between the simulated and experimental spectra is equal to 0.173, equivalent to 2.8%, which is in the same order of magnitude as the mean experimental noise over the whole spectral range.

Figure 11 compares the newly retrieved set to some of the literature ones. As can be seen, the newly retrieved set (in black) coming from this work is the

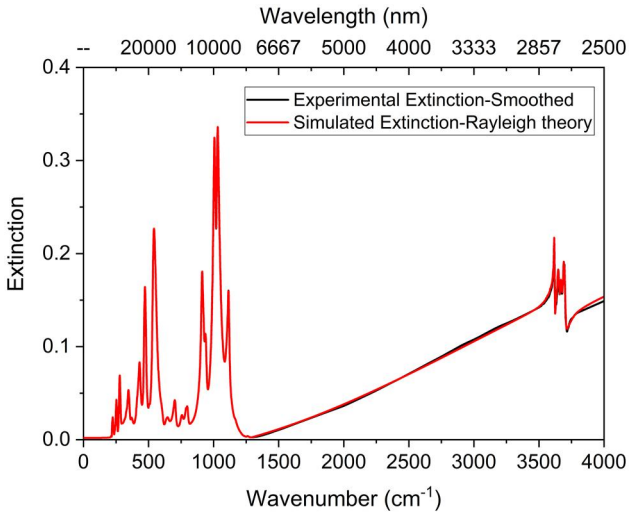

Figure 9. Comparison of the smoothed experimental extinction spectrum (in black) with the simulated extinction spectrum using the CRI retrieved after the Rayleigh theory iterative process between 200 and 4000 cm^{-1}.

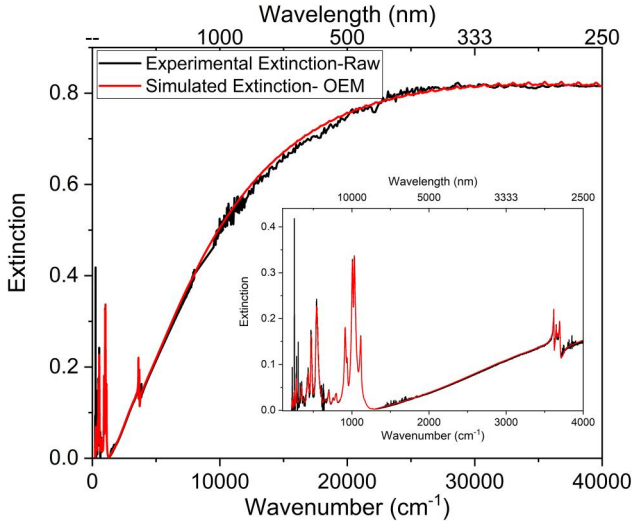

Figure 10. Comparison between the experimental extinction spectrum (in black) and the one simulated by the retrieved CRI using OEM (in red). The inset shows a zoomed portion between 216 and 4000 cm^{-1} highlighting the region from Far Infrared to Mid Infrared.

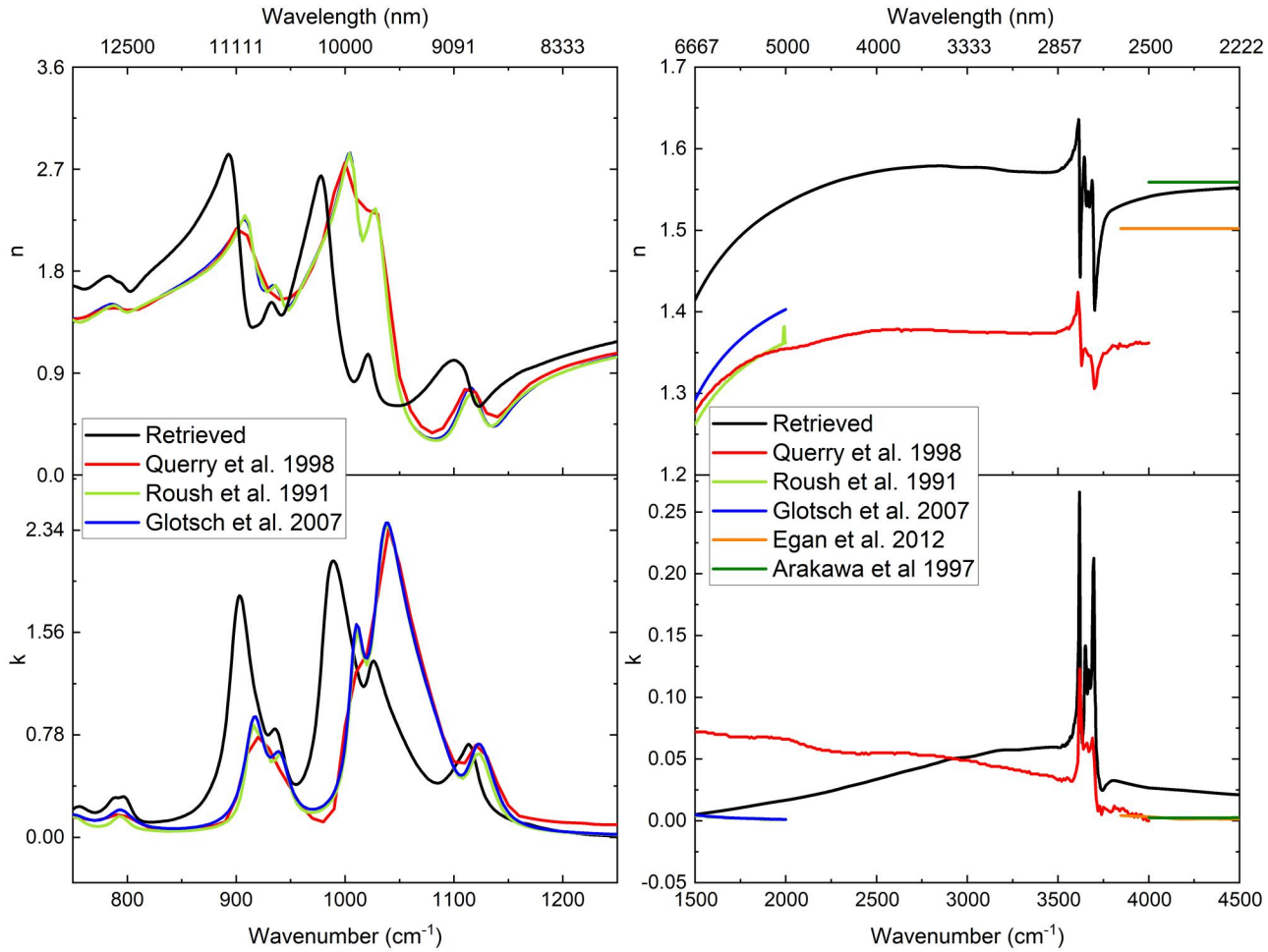

Figure 11. Literature values of the real part (top) and the imaginary part (bottom) of complex refractive indices of kaolinite as well as the newly retrieved CRIs during this study for two spectral ranges. On the left, the spectral range between 750 and 1250 cm^{-1} is shown to highlight the different CRI features in the TIR region. On the right, the spectral range between 1500 and 4500 cm^{-1} is used to show the region where previous literature datasets have a lot of inconsistencies with one another.

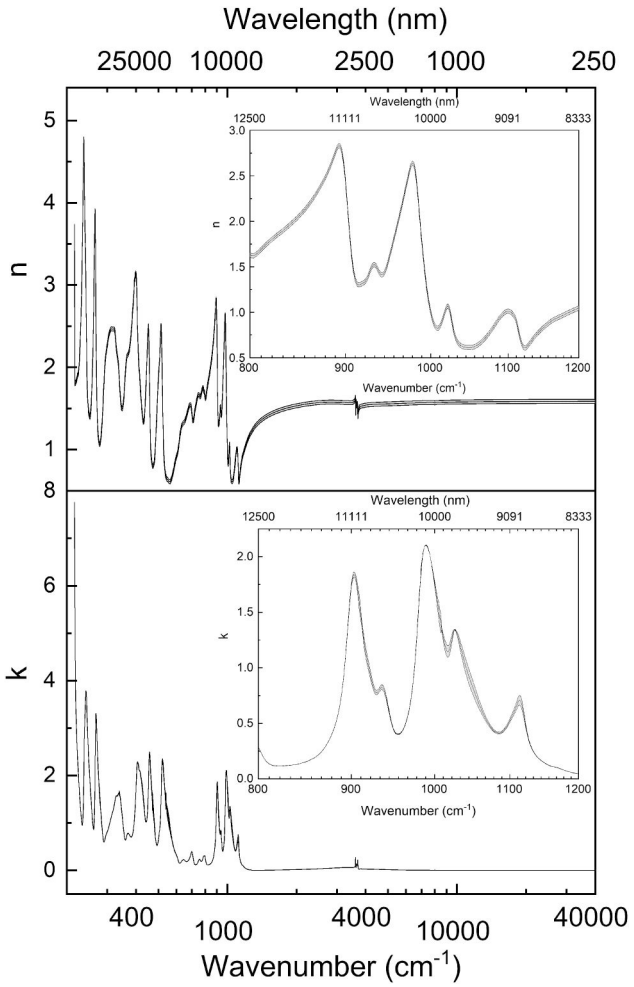

Figure 12. The real part n (top) and the imaginary part κ (bottom) of the refractive index of kaolinite. The grey shading represents the total uncertainties on the retrieved parameters. The insets highlight a zoomed portion between 800 and 1200 cm^{-1} where both Roush, Pollack, and Orenberg (1991) and Querry (1998) have CRI data.

first one to give continuous and coherent CRI values from FIR up to UV. Indeed, the previous literature values of kaolinite CRI are each over limited spectral ranges. Moreover, as can be seen by the right section of the figure, the previous datasets are not consistent with each other. For example, at $\overline{\nu} = 4{,}000\,cm^{-1}$, measurements from Arakawa et al. (1997) of the real part (top right figure) of the refractive index show $n(\overline{\nu}) = 1.559$ while measurements done by Egan (2012) and Querry (1998) have lower values of 1.502 and 1.362, respectively. In both the imaginary and real parts, we can notice clear intensity variations. This is specifically evident when comparing our measurements to the ones of Querry (1998) (right figure). As for the left section of the graph, we notice that we have good consistency in the intensity, however; we observe a strong shift between literature values of both $\kappa(\overline{\nu})$ and $n(\overline{\nu})$ and the newly retrieved set.

3.2. Uncertainties

The advantages of the OEM are that it restores the parameters needed to be retrieved, in our case the CRI, as well as provides a way for characterizing them by a full error budget represented by the total error variance matrix. To properly evaluate the accuracy of the results one must consider the error sources and quantify their impact on these results. The total error on the retrieved CRIs is given by the total error covariance matrix:

$$S_{\text{Total}} = S_{\text{smoothing}} + S_{\text{measurement}} + S_{\text{modparam}} \tag{20}$$

The first term includes the error due to smoothing $S_{\text{smoothing}} = (A - I)S_a(A - I)^T$ that considers the sensitivity of the measurements and the a priori variability to the retrieved parameters $n(\overline{\nu})$ and $k(\overline{\nu})$. In this case, I is the identity matrix and $A = \frac{\partial \hat{x}}{\partial x}$ are the averaging kernels that measure the sensitivity of the retrieved state vector with respect to the true state. The second term is the measurement error $S_{\text{measurement}} = GS_mG^T$ corresponding to the spectral noise where $G = \frac{\partial \hat{x}}{\partial y}$ is the gain matrix representing the sensitivity of the retrieved state vector to the measurement. The final term is the model parameters error $S_{\text{modparam}} = GK_bS_b(GK_b)^T$ and it represents the uncertainties of the non-retrieved SD parameters. Figure 12 illustrates the retrieved CRIs of kaolinite (in black line) as well as their total uncertainties S_{Total} at each wavenumber represented by the shaded area surrounding the retrieved values of $n(\overline{\nu})$ and $\kappa(\overline{\nu})$.

The total uncertainty of $n(\overline{\nu})$ ranges between 0.5% and 4% while that of $\kappa(\overline{\nu})$ is between 0.003% and 11.6%. The average total uncertainties for the real and imaginary parts of the refractive indices are 1.6% and 0.6%, respectively. Most of the uncertainty for the real part of the refractive indices comes from the uncertainty in the SD parameters. It attributes to 99% of the total uncertainty on $n(\overline{\nu})$. As for the imaginary part, the uncertainties coming from the smoothing play the largest part in the total uncertainty, attributing to 70% while the uncertainties due to the forward model of the SD and the spectral noise attribute to 26% and 4%, respectively.

4. Conclusion and perspective

Having reliable CRI values for particles in suspension rather than using pellet or bulk techniques is of major

interest in many fields, specifically in remote sensing. For instance, current and future infrared space missions such as AIRS, IASI, IRS-MTG, or IASI-NG benefit from having CRI datasets for the retrieval of aerosol chemical composition and microphysical parameters. In this context, the future mission FORUM will be the first to perform measurements in the FIR, spectral domain for which the CRIs are very poorly known. In this study, we have improved our experimental setup as well as our numerical algorithm enabling us to retrieve homogenous CRI of aerosols from FIR ($200\,cm^{-1}$) to UV ($40{,}000\,cm^{-1}$) with a spectral resolution of $0.5\,cm^{-1}$. For Kaolinite, the mean total uncertainty for the real and imaginary parts of the retrieved refractive indices is 1.6% and 0.6%, respectively. Moreover, the difference between measured and simulated extinction spectra is estimated at 2.8% which is lower than the error coming from the spectral noise approximated at 4%. The retrieved CRIs of kaolinite as well as the uncertainties at each wavenumber are available on request or online in the supplementary information. The work in progress is dedicated to improving the experimental device used for FIR measurements in order to enhance the signal-to-noise ratio and sensitivity. We aim to extend our studies to other types of aerosols.

Acknowledgments

This work is a contribution to the LabEx CaPPA (Chemical and Physical Properties of the Atmosphere) project funded by the French National Research Agency (ANR) under contract "ANR-11-LABX-0005-01" and to the CPER research project CLIMIBIO/ECRIN funded by the French Ministère de l'Enseignement Supérieur et de la Recherche. The authors thank the Institut on Environmental Sciences (IRePSE, FED 4129, Univ. Lille) for its financial support.

The authors thank Professor Etienne Balan from Institut de Mineralogie, Physique des Materiaux et Cosmochimie (IMPMC) at Sorbonne University for providing us with his experimental data.

Disclosure statement

The authors declare there is no Conflict of Interest.

References

Alalam, P., L. Deschutter, A. Al Choueiry, D. Petitprez, and H. Herbin. 2022. Aerosol mineralogical study using laboratory and IASI measurements: Application to East Asian deserts. *Remote Sens.* 14 (14): 3422. doi: 10.5194/acp-19-15503-2019.

Arakawa, E. T., P. S. Tuminello, B. N. Khare, M. E. Millham, S. Authier, and J. Pierce. 1997. *Measurement of optical properties of small particles*. Oak Ridge, TN: Oak Ridge National Lab.

Atkinson, J. D., B. J. Murray, M. T. Woodhouse, T. F. Whale, K. J. Baustian, K. S. Carslaw, S. Dobbie, D. O'Sullivan, and T. L. Malkin. 2013. The importance of feldspar for ICE nucleation by mineral dust in mixed-phase clouds. *Nature* 498 (7454):355–8. doi: 10.1038/nature12278.

Balan, E., A. M. Saitta, F. Mauri, and G. Calas. 2001. First-principles modeling of the infrared spectrum of kaolinite. *Am. Mineral.* 86 (11–12):1321–30. doi: 10.2138/am-2001-11-1201.

Chen, C., O. Dubovik, G. L. Schuster, M. Chin, D. K. Henze, T. Lapyonok, Z. Li, Y. Derimian, and Y. Zhang. 2022. Multi-angular polarimetric remote sensing to pinpoint global aerosol absorption and direct radiative forcing. *Nat. Commun.* 13 (1):7459. doi: 10.1038/s41467-022-35147-y.

Clarisse, L., D. Hurtmans, A. J. Prata, F. Karagulian, C. Clerbaux, M. D. Mazière, and P.-F. Coheur. 2010. Retrieving radius, concentration, optical depth, and mass of different types of aerosols from high-resolution infrared nadir spectra. *Appl. Opt.* 49 (19):3713–22. doi: 10.1364/AO.49.003713.

DeCarlo, P. F., J. G. Slowik, D. R. Worsnop, P. Davidovits, and J. L. Jimenez. 2004. Particle morphology and density characterization by combined mobility and aerodynamic diameter measurements. Part 1: Theory. *Aerosol. Sci. Technol.* 38 (12):1185–205. doi: 10.1080/02786826.2004.10399461.

Deguine, A., L. Clarisse, H. Herbin, and D. Petitprez. 2023a. Measuring volcanic ash with high-spectral resolution infrared sounders: Role of refractive indices. *IEEE Geosci. Remote Sens. Lett.* 20:1–5. doi: 10.1109/LGRS.2023.3261202.

Deguine, A., D. Petitprez, L. Clarisse, L. Deschutter, K. Fontijn, and H. Herbin. 2023b. Retrieval of refractive indices of ten volcanic ash samples in the infrared, visible and ultraviolet spectral region. *J. Aerosol. Sci.* 167 (1): 106100. doi: 10.1016/j.jaerosci.2022.106100.

Deguine, A., D. Petitprez, L. Clarisse, S. Guđmundsson, V. Outes, G. Villarosa, and H. Herbin. 2020. Complex refractive index of volcanic ash aerosol in the infrared, visible, and ultraviolet. *Appl. Opt.* 59 (4):884. doi: 10.1364/AO.59.000884.

Di Biagio, C., P. Formenti, Y. Balkanski, L. Caponi, M. Cazaunau, E. Pangui, E. Journet, S. Nowak, M. O. Andreae, K. Kandler, et al. 2019. Complex refractive indices and single-scattering albedo of global dust aerosols in the shortwave spectrum and relationship to size and iron vontent. *Atmos. Chem. Phys.* 19 (24):15503–31. doi: 10.5194/acp-19-15503-2019.

Egan, W. 2012. *Optical properties of inhomogeneous materials: Applications to geology, astronomy chemistry, and engineering*. Amsterdam, Netherlands: Elsevier.

Engelbrecht, J. P., H. Moosmüller, S. Pincock, R. K. M. Jayanty, T. Lersch, and G. Casuccio. 2016. Technical note: Mineralogical, chemical, morphological, and optical inter relationships of mineral dust re-suspensions. *Atmos. Chem. Phys.* 16 (17):10809–30. doi: 10.5194/acp-16-10809-2016.

Glotch, T. D., G. R. Rossman, and O. Aharonson. 2007. Mid-infrared (5–100 Mm) reflectance spectra and optical constants of ten phyllosilicate minerals. *ICARUS* 192 (2): 605–22. doi: 10.1016/j.icarus.2007.07.002.

Herbin, H., L. C. Labonnote, and P. Dubuisson. 2013. Multispectral information from TANSO-FTS instrument – part 1: Application to greenhouse gases (CO_2 and CH_4) in clear sky conditions. *Atmos. Meas. Tech.* 6 (11):3301–11. doi: 10.5194/amt-6-3301-2013.

Herbin, H., O. Pujol, P. Hubert, and D. Petitprez. 2017. New approach for the determination of aerosol refractive indices – part I: Theoretical bases and numerical methodology. *J. Quant. Spectrosc. Radiat. Transf.* 200 (1):311–9. doi: 10.1016/j.jqsrt.2017.03.005.

Herbin, H., L. Deschutter, A. Deguine, and D. Petitprez. 2023. Complex refractive index of crystalline quartz particles from UV to thermal infrared. *Aerosol Sci. Technol.* 57 (3):255–65. doi: 10.1080/02786826.2023.2165899.

Hoshino, M., K. Sanematsu, and Y. Watanabe. 2016. Chapter 279 - REE mineralogy and resources. In *Handbook on the physics and vhemistry of rare earths*, eds. B. Jean-Claude and P. K. Vitalij, Vol. 49, 129–291. Including Actinides. Amsterdam, Netherlands: Elsevier.

Hubert, P., H. Herbin, N. Visez, O. Pujol, and D. Petitprez. 2017. New approach for the determination of aerosol refractive indices – part II: Experimental set-up and application to amorphous silica particles. *J. Quant. Spectrosc. Radiat. Transf.* 200 (1):320–7. doi: 10.1016/j.jqsrt.2017.03.037.

Khlystov, A., C. Stanier, and S. N. Pandis. 2004. An algorithm for combining electrical mobility and aerodynamic size distributions data when measuring ambient aerosol. *Aerosol. Sci. Technol.* 38 (1):229–38. doi: 10.1080/02786820390229543.

Kim, J. H., G. W. Mulholland, S. R. Kukuck, and D. Y. H. Pui. 2005. Slip correction measurements of certified PSL nanoparticles using a nanometer differential mobility analyzer (nano-DMA) for knudsen number from 0.5 to 83. *J. Res. Natl. Inst. Stand. Technol.* 110 (1):31–54. doi: 10.6028/jres.110.005.

Kinne, S., M. Schulz, C. Textor, S. Guibert, Y. Balkanski, S. E. Bauer, T. Berntsen, T. F. Berglen, O. Boucher, M. Chin, et al. 2006. An AeroCom initial assessment – optical properties in aerosol component modules of global models. *Atmos. Chem. Phys.* 6 (7):1815–34. doi: 10.5194/acp-6-1815-2006.

Kok, J. F., D. A. Ridley, Q. Zhou, R. L. Miller, C. Zhao, C. L. Heald, D. S. Ward, S. Albani, and K. Haustein. 2017. Smaller desert dust cooling effect estimated from analysis of dust size and abundance. *Nat. Geosci.* 10 (4): 274–8. doi: 10.1038/ngeo2912.

Laskina, O., M. A. Young, P. D. Kleiber, and V. H. Grassian. 2012. Infrared extinction spectra of mineral dust aerosol: Single components and complex mixtures. *Journal of Geophysical Research Atmospheres* 117 (17): 18210. doi: 10.1029/2012JD017756.

Longtin, D. R., E. P. Shettle, J. R. Hummel, and J. D. Pryce. 1988. A *w*ind *d*ependent *d*esert *a*erosol *m*odel: Radiative *p*roperties. Washington, DC: Air Force Geophysics Laboratory, Air Force Systems Command, United States Air Force.

Madejová, J., W. P. Gates, and S. Petit. 2017. Chapter 5 - IR spectra of clay minerals. In *Developments in clay science*, eds. W.P. Gates, J.T. Kloprogge, J. Madejová, and F. Bergaya, Vol. 8, 107–49. *Infrared and Raman Spectroscopies of Clay Minerals*. Amsterdam, Netherlands: Elsevier.

McPheat, R. A., S. F. Bass, D. A. Newnham, J. Ballard, and J. J. Remedios. 2002. Comparison of aerosol and thin film spectra of supercooled ternary solution aerosol. *J.Geophys. Res. Atmos.* 107 (D19):AAC 5-1– 5-8. doi: 10.1029/2001JD000641.

Méndez Harper, J., D. Harvey, T. Huang, J. McGrath, III, D. Meer, and J. C. Burton. 2022. The lifetime of charged dust in the atmosphere. *PNAS Nexus* 1 (5):pgac220. doi: 10.1093/pnasnexus/pgac220.

Mogili, P. K., K. H. Yang, M. A. Young, P. D. Kleiber, and V. H. Grassian. 2007. Environmental aerosol chamber studies of extinction spectra of nineral dust aerosol components: Broadband IR-UV extinction spectra. *J. Geophys. Res.* 112 (D21):D21204. doi: 10.1029/2007JD008890.

Mogili, P. K., K. H. Yang, M. A. Young, P. D. Kleiber, and V. H. Grassian. 2008. Extinction spectra of mineral dust aerosol components in an environmental aerosol chamber: IR resonance studies. *Atmos. Environ.* 42 (8):1752–61. doi: 10.1016/j.atmosenv.2007.11.026.

Nussenzveig, H. M., and W. J. Wiscombe. 1980. EfficiencyfFactors in mie scattering. *Phys. Rev. Lett.* 45 (18):1490–4. doi: 10.1103/PhysRevLett.45.1490.

Osborne, S. R., A. J. Baran, B. T. Johnson, J. M. Haywood, E. Hesse, and S. Newman. 2011. Short-wave and long-wave radiative properties of Saharan dust aerosol. *Quart. J. Royal Meteoro. Soc.* 137 (658):1149–67. doi: 10.1002/qj.771.

Querry, M. R. 1998. Optical *c*onstants of *m*inerals and *o*ther *m*aterials from the *m*illimeter to the *u*ltraviolet. Picatinny Arsenal, NJ: Chemical Research, Development & Engineering Center, U.S. Army Armament Munitions Chemical Command.

Reed, B. E., D. M. Peters, R. McPheat, A. J. A. Smith, and R. G. Grainger. 2017. Mass extinction spectra and size distribution measurements of quartz and amorphous silica aerosol at 0.33–19 Mm compared to modelled extinction using mie, CDE, and T-matrix theories. *J. Quant. Spectrosc. Radiat. Transf.* 199 (1):52–65. doi: 10.1016/j.jqsrt.2017.05.011.

Rodgers, C. D. 2000. *Inverse methods for atmospheric sounding: Theory and practice*. Singapore: World Scientific.

Roush, T., J. Pollack, and J. Orenberg. 1991. Derivation of midinfrared (5–25 Mm) optical constants of some silicates and palagonite. *ICARUS* 94 (1):191–208. doi: 10.1016/0019-1035(91)90150-r.

Satheesh, S. K., and K. K. Moorthy. 2005. Radiative effects of natural aerosols: A review. *Atmos. Environ.* 39 (11): 2089–110. doi: 10.1016/j.atmosenv.2004.12.029.

Savitzky, A., and M. J. E. Golay. 2002. *Smoothing and differentiation of data by simplified least squares procedures.* Research-article. Washington, DC: ACS Publications.

Seinfeld, J. H., and S. N. Pandis. 2006. *Atmospheric chemistry and physics: From air pollution to climate change*. Hoboken, NJ: John Wiley.

Tunega, D., and A. Zaoui. 2020. Mechanical and bonding behaviors vehind the vending mechanism of Kaolinite clay layers. *J. Phys. Chem. C Nanomater. Interfaces.* 124 (13):7432–40. doi: 10.1021/acs.jpcc.9b11274.

Varga, G. 2007. The structure of Kaolinite and metakaolinite. *Epitoanyag - JSBCM.* 59 (1):6–9. doi: 10.14382/epitoanyag-jsbcm.2007.2.

Yu, H., Y. Yang, H. Wang, Q. Tan, M. Chin, R. C. Levy, L. A. Remer, S. J. Smith, T. Yuan, and Y. Shi. 2020. Interannual variability and trends of combustion aerosol and dust in major continental outflows revealed by MODIS retrievals and CAM5 simulations during 2003–2017. *Atmos. Chem. Phys.* 20 (1):139–61. doi: 10.5194/acp-20-139-2020.